ADVANCED MATERIALS

www.advmat.de

Antipulverization Electrode Based on Low-Carbon Triple-Shelled Superstructures for Lithium-Ion Batteries

Lianhai Zu, Qingmei Su, Feng Zhu, Bingjie Chen, Huanhuan Lu, Chengxin Peng, Ting He, Gaohui Du, Pengfei He, Kai Chen, Shihe Yang, Jinhu Yang, and Huisheng Peng**

The realization of antipulverization electrode structures, especially using low-carbon-content anode materials, is crucial for developing high-energy and long-life lithium-ion batteries (LIBs); however, this technology remains challenging. This study shows that SnO_2 triple-shelled hollow superstructures (TSHSs) with a low carbon content (4.83%) constructed by layer-by-layer assembly of various nanostructure units can withstand a huge volume expansion of ≈231.8% and deliver a high reversible capacity of 1099 mAh g^{-1} even after 1450 cycles. These values represent the best comprehensive performance in SnO_2-based anodes to date. Mechanics simulations and in situ transmission electron microscopy suggest that the TSHSs enable a self-synergistic structure-preservation behavior upon lithiation/delithiation, protecting the superstructures from collapse and guaranteeing the electrode structural integrity during long-term cycling. Specifically, the outer shells during lithiation processes are fully lithiated, preventing the overlithiation and the collapse of the inner shells; in turn, in delithiation processes, the underlithiated inner shells work as robust cores to support the huge volume contraction of the outer shells; meanwhile, the middle shells with abundant pores offer sufficient space to accommodate the volume change from the outer shell during both lithiation and delithiation. This study opens a new avenue in the development of high-performance LIBs for practical energy applications.

As one of the current major energy storage technologies, lithium-ion batteries (LIBs) are widely expected to power emerging portable electronics and electric vehicles (EVs).[1–4] To meet this demand, it is necessary to develop high-energy-density LIBs with both long cycling life and high power output. However, LIBs have long suffered from the severe pulverization of anode materials induced by huge volume changes upon Li-ion insertion/extraction, which causes irreversible capacity loss as well as poor cycling stability and rate capability.[5–17] To solve this problem, in most cases, graphitic carbons with good conductivity and excellent mechanical properties were employed as flexible matrices for the anode materials to improve the cycling performance of batteries.[18–29] However, the high carbon content (usually greater than 30%) often results in a capacity decrease due to the low theoretical lithium storage capacity of graphite carbons (≈372 mAh g^{-1}), substantially limiting their practical applications

L. H. Zu, B. J. Chen, Dr. C. X. Peng, Prof. J. H. Yang
School of Chemical Science and Engineering
Tongji University
Shanghai 200092, China
E-mail: yangjinhu@tongji.edu.cn

L. H. Zu, Prof. J. H. Yang
Research Center for Translational Medicine and Key Laboratory of Arrhythmias of the Ministry of Education of China, East Hospital
Tongji University School of Medicine
No. 150 Jimo Road, Shanghai 200120, P. R. China

Dr. Q. M. Su, Prof. G. H. Du
Institute of Physical Chemistry
Zhejiang Normal University
Jinhua 321004, P. R. China

F. Zhu, Prof. P. F. He
School of Aerospace Engineering and Applied Mechanics
Tongji University
Shanghai 200433, China

H. H. Lu, Prof. K. Chen
Center for Advancing Materials Performance from the Nanoscale (CAMP-Nano)
State Key Laboratory for Mechanical Behavior of Materials
Xi'an Jiaotong University
Xi'an 710049, China

T. He
School of Materials Science and Engineering
Tongji University
Shanghai 201804, China

Prof. S. H. Yang
Department of Chemistry
The Hong Kong University of Science and Technology
Clear Water Bay, Kowloon, Hong Kong, China

Prof. H. S. Peng
State Key Laboratory of Molecular Engineering of Polymers
Department of Macromolecular Science and Laboratory of Advanced Materials
Fudan University
Shanghai 200433, China
E-mail: penghs@fudan.edu.cn

The ORCID identification number(s) for the author(s) of this article can be found under https://doi.org/10.1002/adma.201701494.

DOI: 10.1002/adma.201701494

in EVs. One effective way to elevate energy density is to reduce the carbon content in composite anode materials. Nevertheless, it remains a considerable challenge to produce such composite materials with sufficiently low carbon content to ensure high capacity and, simultaneously, maintain a stable architecture for long cycling life.

SnO_2 is an attractive anode material for LIBs due to its high theoretical lithium storage capacity (≈782 mA g^{-1}) and safe working potential (≈0.6 V vs Li+/Li).[17,30–35] However, SnO_2 also suffers from a large volume change (≈250%) and severe structural collapse that result in an unstable solid electrolyte interphase (SEI)[36] and an overall performance deterioration of batteries. To date, SnO_2-based batteries capable of delivering a high reversible capacity (>800 mAh g^{-1}) over 1000 cycles have been extremely limited. In this regard, SnO_2 represents a typical class of LIB anode material facing a serious structural collapse problem that still requires resolution. Therefore, SnO_2 was selected as an example for investigation. In this work, SnO_2 triple-shelled hollow superstructures (TSHSs) with low carbon content (4.83%) assembled hierarchically using various SnO_2-based primary nanostructure units show high lithium storage performance, including a high reversible capacity (1099 mAh g^{-1}) at 0.5 A g^{-1} with a high capacity retention of nearly 100% after 1450 cycles and a high power output (416 mAh g^{-1} at 4 A g^{-1}) with long cycle life (1200 cycles). Further mechanics simulations coupled with in situ transmission electron microscopy (TEM) suggest that such a triple-shelled configuration enables a self-synergistic structure-preservation (SSSP) behavior upon lithiation/delithiation, protecting the TSHSs against collapse and guaranteeing electrode structural integrity during cycling. Therefore, the superior performance of the SnO_2 TSHS is attributed to the following two factors: the optimal structural/composition design of the TSHSs that favors the generation of high-performance LIBs and the SSSP behavior that maintains the structural integrity of the TSHSs throughout the lithiation/delithiation process. The SSSP concept provides a new strategy to construct antipulverization electrodes for high-performance LIBs based on low-carbon-content or carbon-free anode materials.

The synthesis of the TSHSs was realized through the layer-by-layer growth/assembly of various SnO_2 nanounits on the surface of SiO_2 nanospheres, coupled with carbonization/coating of carbon precursors. As shown in **Figure 1**a, the rapid hydrolysis of $Na_2SnO_3{\cdot}3H_2O$ in an ethanol–water solution leads to the dense deposition of SnO_2 nanodots on SiO_2 nanospheres, forming the first shell of SnO_2 nanodots (Figure 1a, step ①). Subsequently, the synchronous hydrolysis of the Sn-precursor and polymerization/carbonization of glucose induce the formation of organic carbon-coated SnO_2 nanodots and their loosely assembled second layer on the surface of the first dense layer (step ②). The double-shelled intermediates, when calcined under N_2 atmosphere for complete carbonization after removing the SiO_2 cores using NaOH solution, transform into the SnO_2 double-shelled hollow superstructures (DSHSs) (Figure 1a, step ③). The double-layer intermediates with exposed OH-rich groups then serve as hydrophilic interfaces for further seeded growth of SnO_2 nanorods, forming the third layer made of radially arrayed nanorods (Figure 1a, step ④). Finally, after deposition of graphenized carbon by chemical vapor deposition in C_2H_2 flow, the SnO_2 TSHSs are produced (Figure 1a, step ⑤). In the following sections, SnO_2 DSHSs were selected and examined together with the SnO_2 TSHSs for comparison, to better understand the role of the triple-shelled configuration of the SnO_2 TSHSs in the structural stability and battery performance.

The structural and elemental analyses of the SnO_2 DSHSs and TSHSs were conducted in detail. A scanning electron microscopy (SEM) image in Figure 1b shows that the SnO_2 DSHSs are monodisperse with rougher surfaces and larger sizes (≈480 nm) relative to the pristine SiO_2 nanospheres (d = 300 nm; Figure S1, Supporting Information). From the TEM image (Figure 1c), it can be seen that the SnO_2 DSHSs are hollow with double shells, namely, a dense inner shell (the first shell) and a loose outer shell (the second shell). As shown in Figure 1d, there is a clear boundary between the two shells. The first shell is ≈25 nm thick, made of densely aggregated SnO_2 nanodots, whereas the second shell possesses a larger shell thickness of ≈60 nm, consisting of loosely packed SnO_2@C nanodots. A high-resolution TEM image (Figure 1d, inset) indicates that the SnO_2 nanodots are coated with a few layers of graphenized carbon. In addition, clear crystal lattices with a d-spacing of 0.335 nm were observed, corresponding to the (110) plane of the tetragonal crystal structure of SnO_2 (JCPDS No. 70-4177). The carbon coating on the SnO_2 nanodots leads to the loose packing of the SnO_2@C nanodots and the formation of the thicker second shells. Compared to the SnO_2 DSHSs, the SnO_2 TSHSs exhibit much rougher surfaces and larger sizes of ≈700 nm after the growth of the third shell of nanorod arrays, as shown in Figure 1e. The hollow characteristics and triple-shelled configuration are further revealed by the TEM image in Figure 1f. The second shells give a relatively lower contrast compared with the other two shells, caused by the lower stacking density of the SnO_2@C nanodots. The triple-shelled configuration can be clearly observed in a selected-area TEM image in Figure 1g; the image shows that the third shell is made of densely assembled SnO_2 nanorods, with a shell thickness of ≈110 nm (Figure 1g, inset at the bottom). The nanorods are estimated to be ≈3–5 nm in diameter and are coated with a few layers (2–3) of graphenized carbon, as judged from the corresponding high-magnification TEM image (Figure 1g and inset on the top).

The presence of C, O, and Sn elements in the SnO_2 TSHSs is evidenced by the corresponding element maps and energy-dispersive X-ray spectroscopy (EDS) analysis (Figure S2a,b, Supporting Information). Line scanning of the TSHS illustrates a shell-dependent distribution of the three elements (Figure S2c,d, Supporting Information), confirming the triple-shelled configuration of the TSHS. The X-ray diffraction (XRD) patterns indicate that DSHSs and TSHSs are both in tetragonal crystal structure (JCPDS No. 70-4177) (Figures S3a and S4a, Supporting Information). The Brunauer-Emmett-Teller (BET) measurements reveal the presence of hierarchical pores, namely, micropores with diameters of ≈3.5 nm and macropores of ≈250 nm (hollow interiors) in the SnO_2 DSHSs and TSHSs (Figures S3b and S4b, Supporting Information). The BET surface areas for the SnO_2 DSHSs and TSHSs are 149.3 and 65.8 m^2 g^{-1}, respectively. The Raman spectra in Figures S3c and S4c (Supporting Information) show typical D and G peaks for

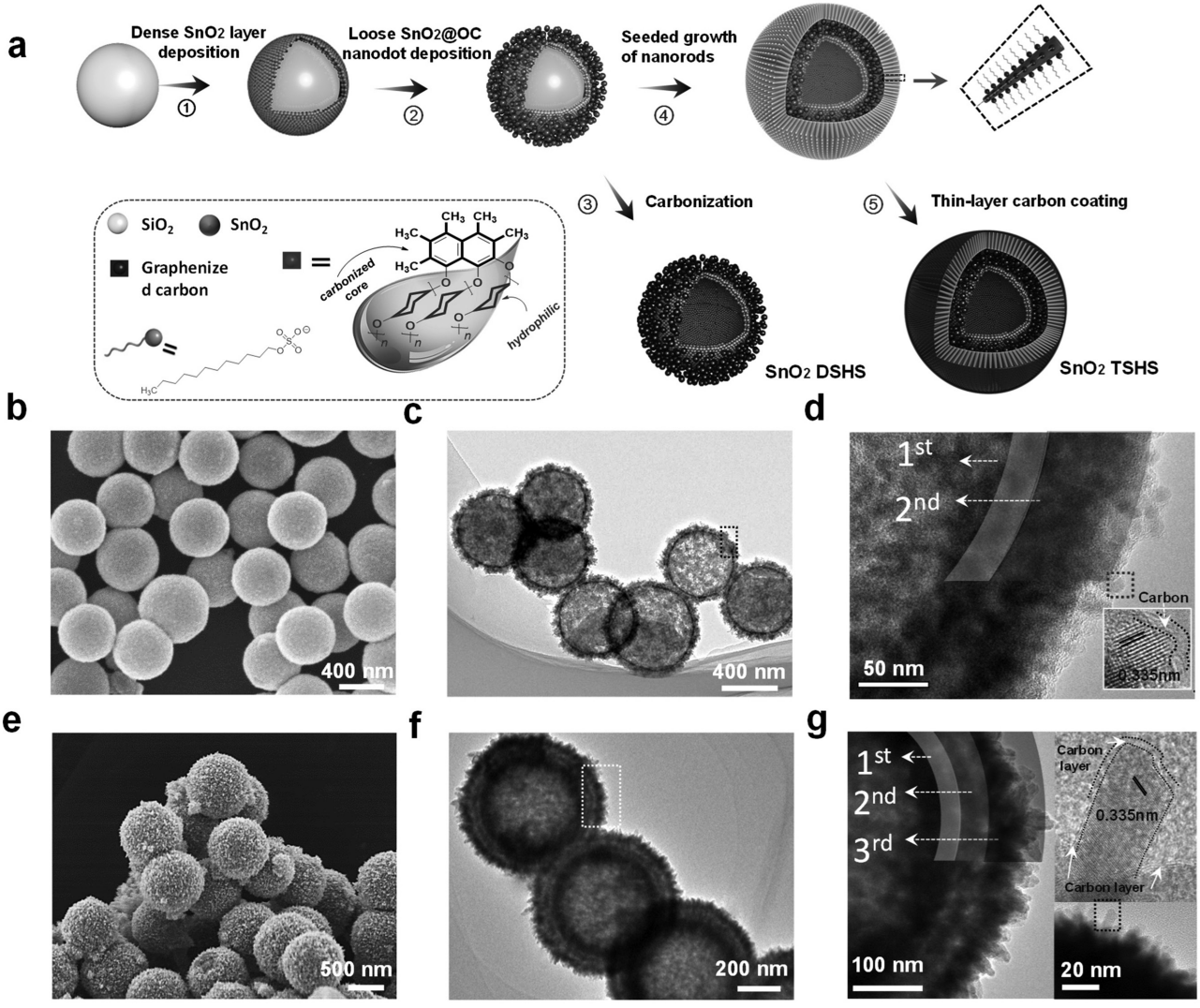

Figure 1. Synthetic route, and morphology and structure characterization for the TSHSs and DSHSs. a) Synthetic route for SnO_2 double-shelled hollow superstructure (DSHS) and triple-shelled hollow superstructures (TSHSs). b) SEM and c,d) TEM images of SnO_2 DSHSs. The inset in (d) is the high-resolution TEM image for an arbitrarily selected SnO_2@C nanodot. e) SEM and f,g) TEM images of SnO_2 TSHSs. The TEM image in (g) corresponds to the rectangle area in (f). The insets in (g) are magnified (right bottom) and high-resolution (upper right) TEM images showing the third shell assembled by SnO_2 nanorod arrays and single nanorod coated with few-layer graphene, respectively.

graphene materials,[37,38] implying that the carbon contained in the samples is graphenized. It is noted that the carbon content in the SnO_2 TSHSs is relatively low (4.83%, mass ratio) compared to that of the SnO_2 DSHSs (35.1%) and other previously reported SnO_2-C composites (Table S1, Supporting Information).[26,27,33,39–46] Therefore, with a set of structural/compositional advantages, such as a high content of SnO_2 active materials (95.17%), a relative high specific surface area (65.8 m^2 g^{-1}), and hierarchical pores, the TSHSs are expected to be a promising anode material for creating high-performance LIBs.

Figure 2 shows the electrochemical performance of the two electrodes based on the SnO_2 DSHSs and TSHSs. The long-term cycling tests measured at a current density of 0.5 A g^{-1} over the voltage range of 0.05–2.5 V are shown in Figure 2a. It can be seen that the SnO_2 TSHS electrode displays much higher specific capacities than the DSHS electrode throughout the cycling. For example, in the first cycle, the SnO_2 TSHS electrode delivers a higher discharge capacity of 2050 mAh g^{-1} as well as a higher initial Coulombic efficiency of 51.2% (Figure S5, Supporting Information) relative to the SnO_2 DSHS electrode (1627 mAh g^{-1}, 44.1%). It is noted that the discharge capacities are two times the theoretical value (≈782 mAh g^{-1}) of SnO_2 material, attributed to the decomposition of the electrolyte forming an SEI film.[36,47] The SnO_2 TSHS electrode shows an upward trend in capacity upon cycling accompanied by a slight fluctuation. The high capacities above 750 mAh g^{-1} are delivered during the entire cycling process. Notably, a capacity of ≈1099 mAh g^{-1} is maintained after 1450 cycles, corresponding to a high capacity retention of ≈104.7%. For the SnO_2 DSHS electrode, however, a constant capacity decrease occurred throughout the cycling process, resulting in a low capacity of 155 mAh g^{-1} and a low capacity retention of 21.6% after

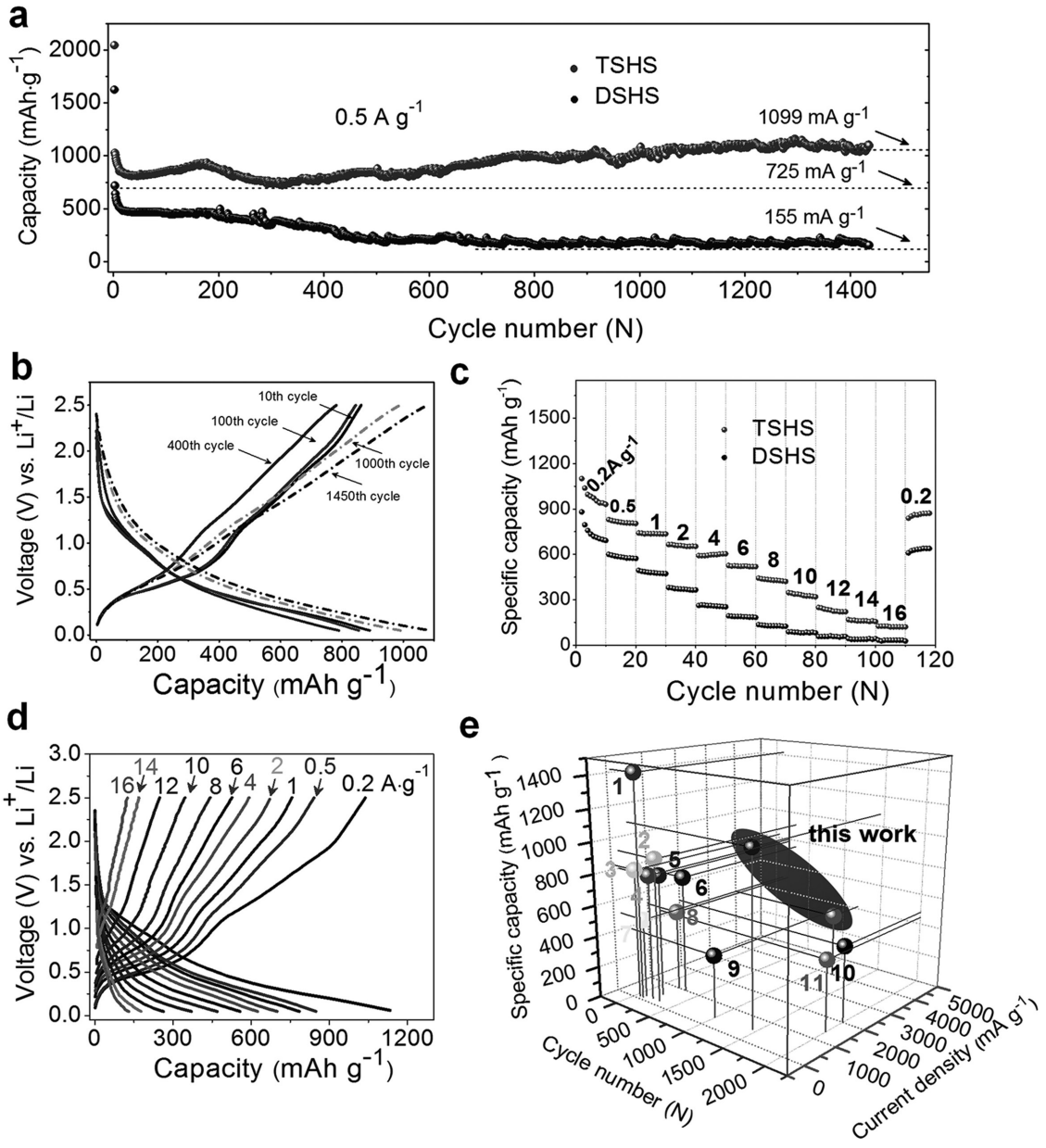

Figure 2. Battery performance of the TSHSs and the DSHSs. a) Cycling performance of the SnO_2 DSHS and TSHS electrodes at 0.5 A g^{-1} between 2.5 and 0.05 V in coin-type half cells at room temperature. b) Galvanostatic charge–discharge profiles of SnO_2 TSHS electrode at the 10th, 100th, 400th, 1000th, and 1450th cycles at 0.5 A g^{-1}. c) Rate capability of the SnO_2 DSHS and TSHS electrodes at current densities between 0.2 and 16 A g^{-1}, respectively. d) Galvanostatic charge–discharge profiles of the SnO_2 TSHS electrode at current densities between 0.2 and 16 A g^{-1}. e) Comprehensive performance comparison (specific capacity vs cycle vs current density) of SnO_2 TSHS-based LIB with other SnO_2 anode-based LIBs.

cycling, only ≈14.3% and ≈20% of the SnO_2 TSHS electrode values, respectively. The trend in capacity change is reflected in the galvanostatic charge/discharge profiles of the SnO_2 TSHS electrode (Figure 2b). Moreover, at higher current densities of 1 and 2 A g^{-1}, the TSHS electrode can also deliver high capacities almost twice those of the DSHS electrode (Figure S6, Supporting Information).

In addition, the SnO_2 TSHS electrode manifests a remarkable rate capability compared to the DSHS electrode. As shown in Figure 2c and Table S2 (Supporting Information), the SnO_2 TSHS electrode demonstrates high reversible capacities, from ≈931 mAh g^{-1} at 0.2 A g^{-1} to 120 mAh g^{-1} at 16 A g^{-1}, which is ≈34%–344% higher than those of the SnO_2 DSHS electrode. Moreover, when the current density returns from 16 A g^{-1} to the initial 0.2 A g^{-1} after 120 cycles, the SnO_2 TSHS electrode still delivers a high capacity of 872 mAh g^{-1}, with a capacity retention of ≈93.7%. The outstanding rate capability of the SnO_2 TSHS electrode is also confirmed by the voltage profiles tested at the corresponding current densities (Figure 2d). Moreover, to further evaluate the long-cycle high-power performance, long-term cycling tests (up to 1200 cycles) at a high current density of 4 A g^{-1} were applied to the two electrodes.

It can be seen in Figure S7 (Supporting Information) that the SnO_2 TSHS electrode is generally stable during the cycling and displays an upward trend in capacity in the latter 1000 cycles from the 200th to the 1200th cycle. The capacity finally stabilizes at 416 mAh g^{-1} with a capacity retention of 57.5% after 1200 cycles, which far surpasses the remaining capacity (123 mAh g^{-1}) for the SnO_2 DSHS electrode, as well as its corresponding capacity retention (25.7%). To the best of our knowledge, the superior performance of the SnO_2 TSHS electrode, such as the ultrahigh capacity (1099 mAh g^{-1} at 0.5 A g^{-1}) remaining after long-term cycling (1450 cycles), with a capacity retention of nearly 100%, and its high power output (416 mAh g^{-1} at 4 A g^{-1}) with long cycle life (1200 cycles), is among the best comprehensive performances for SnO_2-based anode materials reported so far. Performance comparisons between the LIBs based on the SnO_2 TSHSs and other SnO_2 anode materials are provided in Figure 2e and Table S1 (Supporting Information). In addition, it is found that the high capacity uptake of the SnO_2 TSHSs are derived from their triple-shelled configuration that enables higher reaction reversibility with a higher theoretical capacity, which is analyzed and discussed in detail based on peformance comparisons and cyclic voltammetry studies (Figures S8–S10 in S1 and Figures S11–S13 in S2, Supporting Information).[48–51]

It is found that the TSHSs can withstand huge volume change upon lithiation/delithiation after even 1450 cycles, whereas the DSHSs fail. Unlike the stable SEI film formed on the TSHSs, the collapse process of the DSHSs induces repeated formation of new SEI films around the surface of DSHS fragments, leading to unstable lithiation/delithiation interfaces, as illustrated in **Figure 3**a. Figure 3b shows the TEM images of the TSHSs undergoing lithiation/delithiation for 1450 cycles. It can be seen that the morphology of the TSHSs is preserved well (Figure 3b, inset, and Figure S14, Supporting Information), with a thin SEI film (≈20 nm) covering the surface of the outer shell. The existence of SEI films for the TSHSs and DSHSs are confirmed by XPS analyses shown in Figures S15 and S16 (Supporting Information), where some typical X-ray photoelectron spectroscopy (XPS) peaks correspond to LiF, PF^-_6, and C=O bonds that are generally considered as the main compositions of SEI film formed from the decomposition of the electrolyte of $LiPF_6$. At a high magnification, it is seen that the outer shells consist of uniform nanodots, indicating that the nanorods in the outer shell have turned into ultrasmall nanodots after the long-term cycling. Some SnO_2 nanodots with crystalline domains of ≈2–4 nm are observed in the outer shell, without an SEI film existing on the nanodot surfaces (Figure 3c). By contrast, the DSHS is collapsed into pieces with cracks during cycling (Figure 3d and Figure S14, Supporting Information); the new surfaces of the fragments generated during the collapse process are coated with abundant SEI film. The collapse of the DSHSs leads to the pulverization of the DSHS electrode, which inevitably induces the direct loss of active materials and an unstable SEI film repeatedly being formed at newly generated interfaces, thus resulting in a capacity decrease and cycling instability.[7,52]

In situ TEM was employed to monitor the real-time structural evolution of the TSHS and DSHS electrodes during a lithiation/delithiation cycle. The setup for the in situ TEM device is illustrated in Figure 3f, where a selected TSHS or DSHS connected to the Au tip serves as a working electrode and a piece of Li coated with Li_2O on W nanowire tip works as a counter electrode. As shown in Figure 3g and Movie S1 (Supporting Information), the TSHS expands immediately after application of voltage bias. The radius of the TSHS increases gradually from the initial 360 nm to the maximum of 468 nm after 350 s of Li deposition and then shrinks to the minimum 367 nm after another 110 s of Li extraction. It is noted that the hollow interior also undergoes an "expansion/contraction" process in response to lithiation/delithiation, implying a synchronous expansion/contraction behavior of the three shells. It can also be found that some nanorods in the outer shell transform into smaller nanodots after the cycle, and the triple-shelled configuration of the TSHS is still well preserved. For the DSHS, it collapsed in 5 s during the volume shrinking process after 150 s of volume expansion with the radius increasing from 254 to 310 nm (Figure 3h and Movie S2, Supporting Information). Some key values, such as volume changes as well as volume expansion ratios during lithiation for each shell of the DSHS and TSHS, were calculated and listed in Table S3 in S3 (Supporting Information), in terms of the data obtained from in situ TEM observation. As can be seen, the first, second, and third shells for the TSHS expanded to 145.1%, 187.9%, and 242% (volume expansion ratio, $r^i_{v/v}$), respectively, with a general expansion ratio ($R_{v/v}$) of 231.8%. Relatively, the DSHS has a higher $r^i_{v/v}$ of 157.4% and 208.6% in the first and second shells, respectively, but a lower $R_{v/v}$ of 188.1%. Theoretically, the volume expansion ratio is proportional to the extent of lithiation, and a higher volume expansion ratio corresponds to a higher lithiation degree with a higher capacity. As a consequence, the TSHS can deliver higher reversible capacities (Figure 2c), due to its higher general volume expansion ratio (231.8%) than that (188.1%) of the DSHS, which even approaches the theoretical value of 250%.[53,54] In addition, the existence of the third shell in TSHSs can reduce the lithiation extent of both the first shell (145.1% vs 157.4%) and the second shell (187.9% vs 208.6%), thereby preventing the collapse of the two shells as well as the TSHSs. Specifically, the third shell contributes ≈92.57% capacity to the total, whereas the other two shells give less than 8%, according to the calculations on the capacity contribution ratio ($R^i_{\Delta V/\Delta V}$) of individual shells for the TSHS. The calculations support quantitatively the electrochemical results that demonstrate that the TSHSs can uptake a higher capacity and are more stable against lithiation/delithiation.

It is still surprising that the triple-shelled configuration of the SnO_2 TSHSs, with a low carbon content of 4.83%, can withstand huge volume expansion of up to 242% after thousands of cycles. The test of in situ mechanical TEM on an individual TSHS was conducted (Figure S17 in S4, Supporting Information). The load-displacement curve of a typical compression test on an individual TSHS shows that even with the formation of the crack, the loading force kept increasing, and the TSHS does not fracture or break into pieces as commonly observed in other cases, demonstrating an antipulverization structure of TSHS. To more deeply understand why the TSHS is stable during the lithiation process, an elastic–plastic model coupled to Li diffusion was adopted to evaluate the lithiation-induced

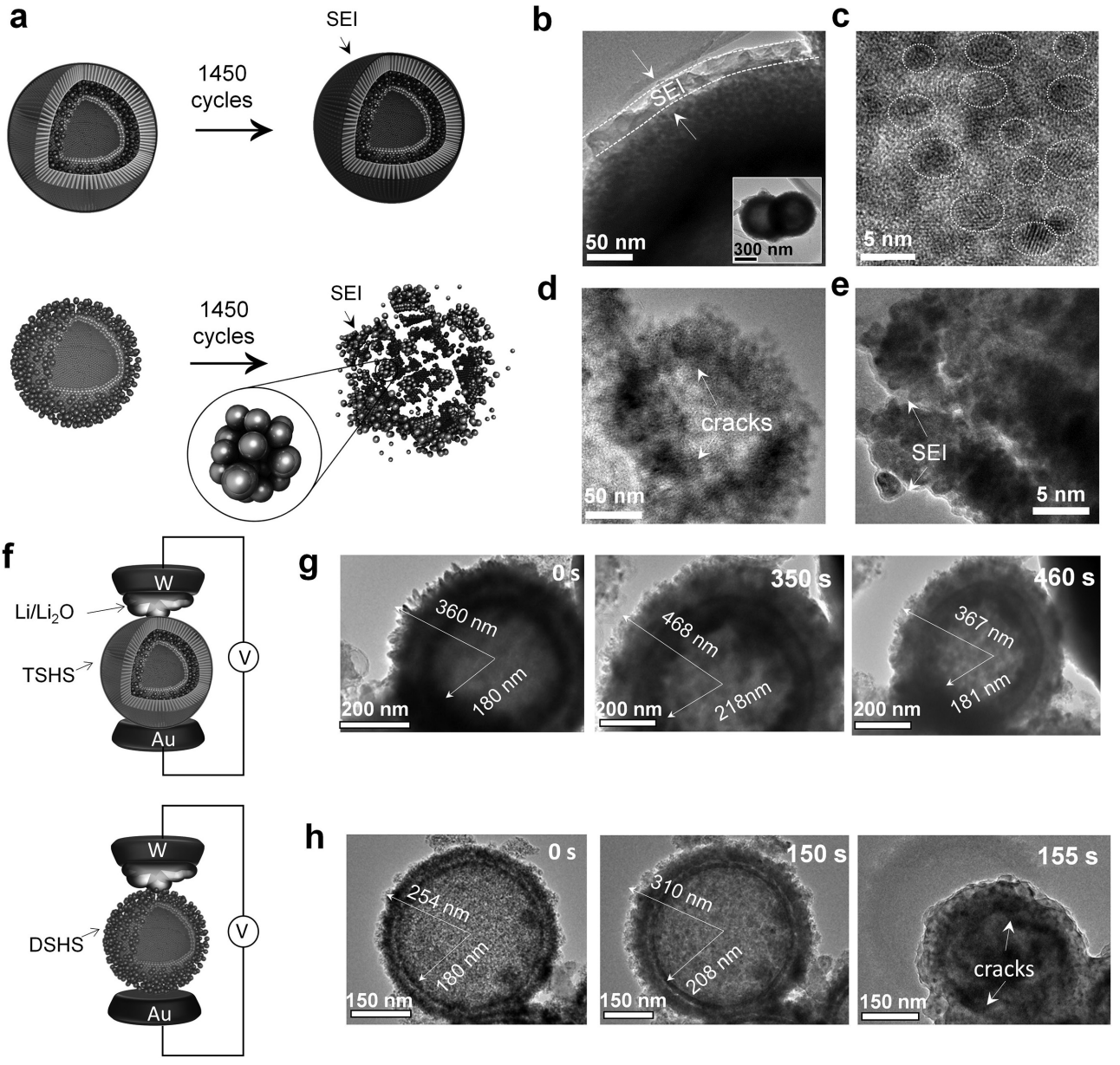

Figure 3. Structure stability study of the TSHS and DSHS. a) Schematic illustration of final architecture state of SnO_2 TSHS and DSHS upon lithiation/delithiation up to 1450 cycles. b) Low and c) high-resolution TEM images of a SnO_2 TSHS after 1450 cycles. d) Low and e) high-resolution TEM images of a SnO_2 DSHS after 1450 cycles. f) Schematic of the dry cells based on a SnO_2 TSHS and a DSHS for in situ TEM study. Time-lapse TEM images for g) a SnO_2 TSHS and h) a DSHS during a full lithiation–delithiation process with an applied voltage of ±3 V between W and Au electrodes. Scale bars in (g) and (h) are 200 and 150 nm, respectively.

deformation and stress states (**Figure 4**, and Figure S18 in S4 in supporting information). In the simulations, we are more attentive to tensile stress as it is the key factor for the collapse of the electrode structures. Figure 4a shows the morphology evolution of TSHSs during the lithiation process, where colors from blue to red correspond to different lithiation extents (or Li-ion concentrations) from low lithiation to high lithiation, respectively. Initially, the Li-ion concentration in the TSHS structure is ≈0 (0 s). Afterward, partial lithiation of the TSHS occurs, leading to some structural deformation on the side contacting the electrode (120 s). This deformation continues until the TSHS is fully lithiated at 350 s. The stress simulation after the lithiation in Figure 4b shows that the third shell experiences very low tensile stress, despite a huge compressive stress (up to ≈230 MPa) in the region adjacent to the second shell. The second shell is almost in a stress-free state due to the existence of sufficient internanodot space to effectively relieve both tensile and compressive stress. For the first shell, a tensile stress (≈150 MPa) generates dramatically near the region between the first and second shells. Figure 4c presents the stress state for the TSHS at different lithiation extents and times during the lithiation process. It can be found that a tensile

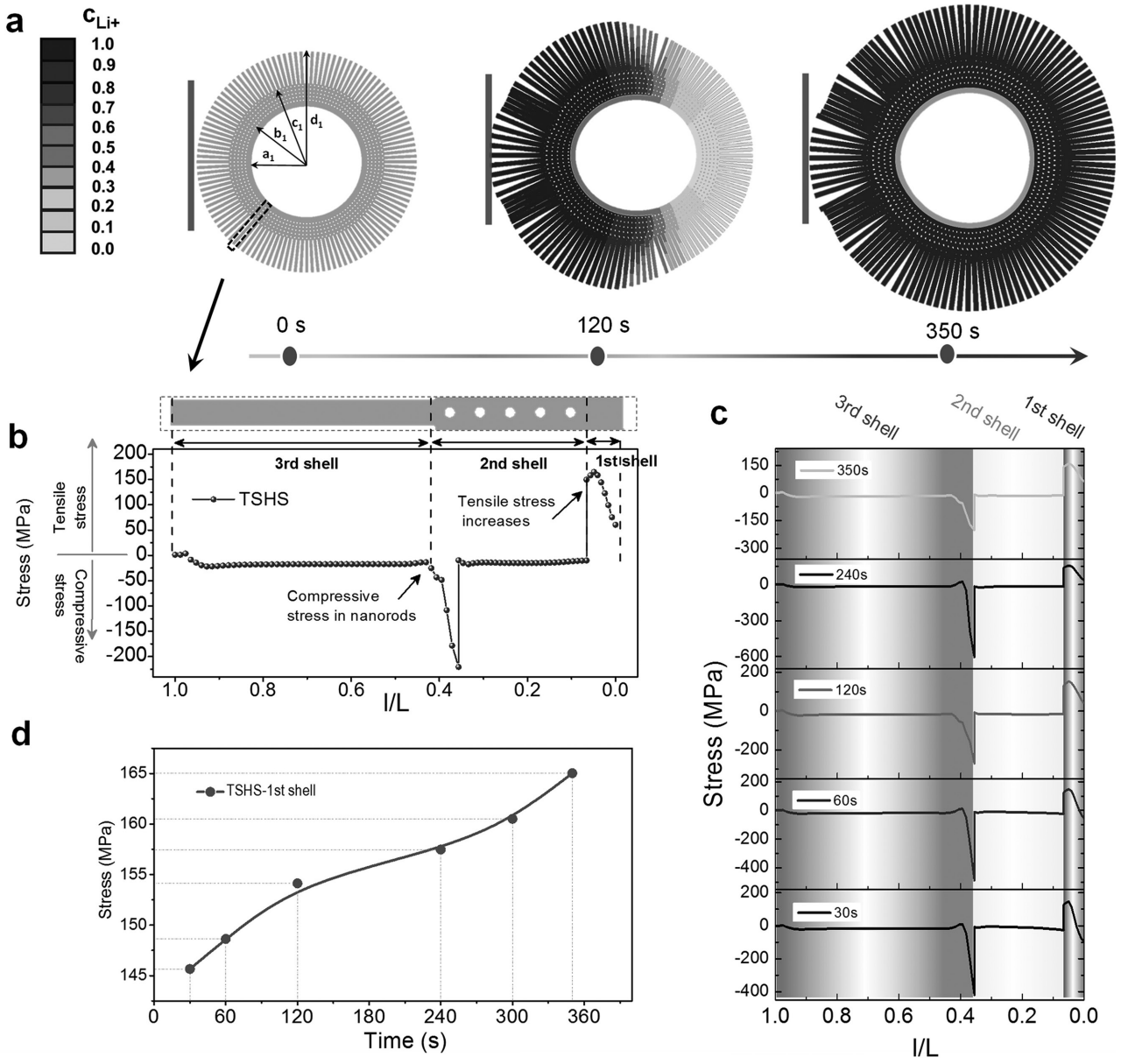

Figure 4. Mechanics simulations for the TSHS during the lithiation process. a) Maximum principal stress contours on deformed shapes of TSHS during lithiation at 0, 120, and 350 s. Normalized Li concentration, c_{Li}, defined as the actual Li concentration divided by the Li concentration in the fully lithiated state. The lithiation reaction front is located at the interface between pristine (blue) and lithiated (red) phases. b) Evolution of stress in the three shells of a TSHS after lithiation. The shell thickness, from the first shell to the third shell, is normalized as 0 to 1. c) Hoop stress evolution of the first, second, and third shells of the TSHS during lithiation. d) The peak value of tensile stress in the first shell as a function of time.

stress exists in the first shell throughout the lithiation, with the corresponding peak values increasing monotonically with lithiation proceeding (Figure 4d). For the DSHS, a similar structural deformation occurred during lithiation, as shown in Figure S18a (Supporting Information). However, the tensile stress behavior in the first shell during lithiation is different from that of the TSHS (Figure S18b–d, Supporting Information). As shown in Figure S18d (Supporting Information), the peak values of the tensile stress decrease continuously through the lithiation process from ≈185 to ≈110 MPa, which indicates that the DSHS may collapse at the very beginning of the lithiation process. It is noted that the DSHS undergoes a higher maximum tensile stress (≈185 MPa) in the first shell than that (≈165 MPa) of the TSHS, demonstrating that the THSH possesses better structural stability due to the triple-shelled configuration.

It is noteworthy that the DSHS collapsed during volume shrinking, instead of volume expanding, in the delithiation process (Figure 3h, in situ TEM observation). This result implies that a high tensile stress should be produced during the delithiation process and lead to the collapse of the DSHS. The stress states for the sample, however, are challenging to

simulate due to the difficulty of modeling delithiation processes. For the TSHS, a huge tensile stress during the delithiation process is also considered to be generated, especially in the third shell, which is the most lithiated and expanded. As seen in Figure 3g, compared with the initial state before cycling, the space of the second shell of the TSHS after delithiation is clearly compressed, whereas the position of the first shell is almost unchanged (R1, from initial 180 nm to final 181 nm). This finding demonstrates that the third shell has experienced tremendous volume shrinkage and huge tensile stress that may transfer to the first shell via the second shell. The first shell is underlithiated in the lithiation process, observed from in situ high-resolution TEM images of the TSHS in Figure S19 (Supporting Information). The first shell with a low lithiation extent and a low volume change may serve as a robust and stable inner core to support the shrunken third shell and alleviate the stress in the third shell, protecting the third shell as well as the TSHS from collapse. Certainly, the second shell with abundant pores may also be crucial for buffering the volume shrinkage from the third shell. Consequently, the TSHS can effectively resist the huge volume contraction.

Taking both lithiation and delithiation into consideration, it can be deduced that a self-synergistic structure-preservation behavior occurs in the TSHSs during cycling: as illustrated in Figure S20a (Supporting Information), during the lithiation process, the third shells that contribute to the major capacity prevent the overlithiation and the breaking of the first shells; in turn, in the delithiation process, the underlithiated first shells work as a robust core to support the huge volume contraction of the third shells; and the second shells with abundant pores offer sufficient space to accommodate the volume change from the third shell during both lithiation and delithiation.[55] By contrast, for the DSHS, without the third shells that consume most of the lithium ions released from the cathode, the first inner shells are fully lithiated with more volume expansion in the lithiation process, and subsequently undergo tremendous volume shrinkage and huge tensile stress during delithiation, which leads to the collapse of the first shells as well as the DSHSs (Figure S20b, Supporting Information).

In summary, SnO_2 TSHSs were fabricated via the layer-by-layer assembly of various SnO_2 structure units. SnO_2 TSHSs exhibit outstanding lithium-storage performance as an LIB anode, such as high capacity, long cycling life, and high rate capability. The superior comprehensive performance is ascribed to the unique structural design of the TSHSs and the SSSP mechanism that maintains the structural integrity of the TSHSs during the lithiation/delithiation process. The SSSP behavior is derived from the triple-shelled configuration of the THSHs, which is demonstrated by in situ TEM and mechanics simulations. This study establishes a prototypical model to recognize the specific working mechanism involved in the hollow or multishelled structure anodes that have been widely employed for LIBs. This novel SSSP concept provides a new strategy to construct antipulverization electrodes, using carbon-free anode materials or those containing less carbon, for the development of high-performance LIBs with high energy, long cycle life, and high power.

Supporting Information

Supporting Information is available from the Wiley Online Library or from the author.

Acknowledgements

This work was financially supported by the National Natural Science Foundation (Grant Nos. 21273161 and 51671154), the Natural Science Foundation of Shanghai (Grant No. 17ZR1447800), the Program for Professor of Special Appointment (Eastern Scholar) at Shanghai Institutions of Higher Learning, Shanghai Innovation Program (Grant No. 13ZZ026), Hundred Youth Talent Plan of Tongji University, the Fundamental Research Funds for the Central Universities, the National Key Research and Development Program of China (Grant No. 2016YFB0700404), and the International Joint Laboratory for Micro/Nano Manufacturing and Measurement Technologies.

Conflict of Interest

The authors declare no conflict of interest.

Keywords

antipulverization, carbon, lithium-ion batteries, SnO_2, triple-shelled structure

Received: March 16, 2017
Revised: May 4, 2017
Published online: June 21, 2017

[1] B. Dunn, H. Kamath, *Science* **2011**, *334*, 928.
[2] B. Kang, G. Ceder, *Nature* **2009**, *458*, 190.
[3] M. K. Song, S. Park, F. M. Alamgir, J. Cho, M. Liu, *Mater. Sci. Eng. Rep.* **2011**, *72*, 203.
[4] M. Armand, J. M. Tarascon, *Nature* **2008**, *451*, 652.
[5] X. Li, M. Gu, S. Hu, R. Kennard, P. Yan, X. Chen, C. Wang, M. J. Sailor, J. G. Zhang, J. Liu, *Nat. Commun.* **2014**, *5*, 4105.
[6] J. Liu, P. Kopold, C. Wu, P. A. van Aken, J. Maier, Y. Yu, *Energy Environ. Sci.* **2015**, *8*, 3531.
[7] Y. Li, K. Yan, H. W. Lee, Z. Lu, N. Liu, Y. Cui, *Nat. Energy* **2016**, *1*, 15029.
[8] J. Wang, H. Tang, L. Zhang, H. Ren, R. Yu, Q. Jin, J. Qi, D. Mao, M. Yang, Y. Wang, P. Liu, Y. Zhang, Y. Wen, L. Gu, G. Ma, Z. Su, Z. Tang, H. Zhao, D. Wang, *Nat. Energy* **2016**, *1*, 16050.
[9] Z. Y. Wang, L. Zhou, X. W. Lou, *Adv. Mater.* **2012**, *24*, 1903.
[10] Y. J. Hong, M. Y. Son, Y. C. Kang, *Adv. Mater.* **2013**, *25*, 2279.
[11] N. Liu, Z. D. Lu, J. Zhao, M. T. McDowell, H. W. Lee, W. T. Zhao, Y. Cui, *Nat. Nanotechnol.* **2014**, *9*, 187.
[12] L. Zhou, D. Y. Zhao, X. W. Lou, *Adv. Mater.* **2012**, *24*, 745.
[13] J. Liu, H. Xia, D. F. Xue, L. Lu, *J. Am. Chem. Soc.* **2009**, *131*, 12086.
[14] G. Q. Tan, F. Wu, Y. F. Yuan, R. J. Chen, T. Zhao, Y. Yao, J. Qian, J. R. Liu, Y. S. Ye, R. Shahbazian-Yassar, J. Lu, K. Amine, *Nat. Commun.* **2016**, *7*, 11774.
[15] M. J. Zhou, Y. C. Liu, J. Chen, X. L. Yang, *J. Mater. Chem. A* **2015**, *3*, 1068.
[16] W. W. Xu, K. N. Zhao, C. J. Niu, L. Zhang, Z. Y. Cai, C. H. Han, L. He, T. Shen, M. Y. Yan, L. B. Qu, L. Q. Mai, *Nano Energy* **2014**, *8*, 196.

[17] S. Chen, M. Wang, J. F. Ye, J. G. Cai, Y. R. Ma, H. H. Zhou, L. M. Qi, *Nano Res.* **2013**, *6*, 243.
[18] H. Liu, W. Li, D. Shen, D. Zhao, G. Wang, *J. Am. Chem. Soc.* **2015**, *137*, 13161.
[19] R. Y. Zhang, Y. J. Du, D. Li, D. K. Shen, J. P. Yang, Z. P. Guo, H. K. Liu, A. A. Elzatahry, D. Y. Zhao, *Adv. Mater.* **2014**, *26*, 6749.
[20] J. Liang, X.Y. Yu, H. Zhou, H. B. Wu, S. J. Ding, X. W. Lou, *Angew. Chem., Int. Ed.* **2014**, *53*, 12803.
[21] W. Ni, Y. B. Wang, R. Xu, *Part. Part. Syst. Charact.* **2013**, *30*, 873.
[22] L. Zhang, H. B. Wu, B. Liu, X. W. Lou, *Energy Environ. Sci.* **2014**, *7*, 1013.
[23] R. Z. Hu, H. Y. Zhang, J. W. Liu, D. C. Chen, L. C. Yang, M. Zhu, M. L. Liu, *J. Mater. Chem. A* **2015**, *3*, 15097.
[24] S. M. Hwang, Y. G. Lim, J. G. Kim, Y. U. Heo, J. H. Lim, Y. Yamauchi, M. S. Park, Y. J. Kim, S. X. Dou, J. H. Kim, *Nano Energy* **2014**, *10*, 53.
[25] L. Zhang, G. Q. Zhang, H. B. Wu, L. Yu, X. W. Lou, *Adv. Mater.* **2013**, *25*, 2589.
[26] D. N. Wang, J. L. Yang, X. F. Li, D. S. Geng, R. Li, M. Cai, T. K. Sham, X. L. Sun, *Energy Environ. Sci.* **2013**, *6*, 2900.
[27] S. H. Yu, D. J. Lee, M. Park, S. G. Kwon, H. S. Lee, A. Jin, K. S. Lee, J. E. Lee, M. H. Oh, K. Kang, Y. E. Sung, T. Hyeon, *J. Am. Chem. Soc.* **2015**, *137*, 11954.
[28] J. Qin, C. N. He, N. Q. Zhao, Z. Y. Wang, C. S. Shi, E. Z. Liu, J. J. Li, *ACS Nano* **2014**, *8*, 1728.
[29] C. X. Peng, B. D. Chen, Y. Qin, S. H. Yang, C. Z. Li, Y. H. Zuo, S. Y. Liu, J. H. Yang, *ACS Nano* **2012**, *6*, 1074.
[30] X. W. Lou, C. M. Li, L. A. Archer, *Adv. Mater.* **2009**, *21*, 2536.
[31] C. Wang, Y. Zhou, M. Y. Ge, X. B. Xu, Z. L. Zhang, J. Z. Jiang, *J. Am. Chem. Soc.* **2010**, *132*, 46.
[32] V. Aravindan, K. B. Jinesh, R. R. Prabhakar, V. S. Kale, S. Madhavi, *Nano Energy* **2013**, *2*, 720.
[33] J. Lin, Z. W. Peng, C. S. Xiang, G. D. Ruan, Z. Yan, D. Natelson, J. M. Tour, *ACS Nano* **2013**, *7*, 6001.
[34] M. S. Park, G. X. Wang, Y. M. Kang, D. Wexler, S. X. Dou, H. K. Liu, *Angew. Chem., Int. Ed.* **2007**, *46*, 750.
[35] Y. C. Jiao, D. D. Han, Y. Ding, X. F. Zhang, G. N. Guo, J. H. Hu, D. Yang, A. G. Dong, *Nat. Commun.* **2015**, *6*, 6420.
[36] R. Hu, D. Chen, G. Waller, Y. Ouyang, Y. Chen, B. Zhao, B. Rainwater, C. Yang, M. Zhu, M. Liu, *Energy Environ. Sci.* **2016**, *9*, 595.
[37] J. Biener, S. Dasgupta, L. Shao, D. Wang, M. A. Worsley, A. Wittstock, J. R. I. Lee, M. M. Biener, C. A. Orme, S. O. Kucheyev, B. C. Wood, T. M. Willey, A. V. Hamza, J. Weissmüller, H. Hahn, T. F. Baumann, *Adv. Mater.* **2012**, *24*, 5083.
[38] C. X. Peng, Z. B. Wen, Y. Qin, L. Schmidt-Mende, C. Z. Li, S. H. Yang, D. L. Shi, J. H. Yang, *ChemSusChem* **2014**, *7*, 777.
[39] D. Kang, Q. Liu, M. Chen, J. Gu, D. Zhang, *ACS Nano* **2016**, *10*, 889.
[40] Y. Z. Su, S. Li, D. Q. Wu, F. Zhang, H. W. Liang, P. F. Gao, C. Cheng, X. L. Feng, *ACS Nano* **2012**, *6*, 8349.
[41] A. Jahel, C. M. Ghimbeu, L. Monconduit, C. Vix-Guterl, *Adv. Energy Mater.* **2014**, *4*, 1400025.
[42] B. Luo, T. F. Qiu, L. Hao, B. Wang, M. H. Jin, X. L. Li, L. J. Zhi, *J. Mater. Chem. A* **2016**, *4*, 362.
[43] C. Guan, X. Wang, Q. Zhang, Z. Fan, H. Zhang, H. J. Fan, *Nano Lett.* **2014**, *14*, 4852.
[44] B. Huang, X. H. Li, Y. Pei, S. Li, X. Cao, R. C. Masse, G. Z. Cao, *Small* **2016**, *12*, 1945.
[45] L. Xia, S. Q. Wang, G. X. Liu, L. X. Ding, D. D. Li, H. H. Wang, S. Z. Qiao, *Small* **2016**, *12*, 853.
[46] K. Zhao, L. Zhang, R. Xia, Y. Dong, W. Xu, C. Niu, L. He, M. Yan, L. Qu, L. S. Mai, *Small* **2016**, *12*, 588.
[47] D. Deng, J. Y. Lee, *Chem. Mater.* **2008**, *20*, 1841.
[48] B. B. Jiang, C. Han, B. Li, Y. J. He, Z. Q. Lin, *ACS Nano* **2016**, *10*, 2728.
[49] S. P. Wu, C. P. Han, J. Iocozzia, M. J. Lu, R. Y. Ge, R. Xu, Z. Q. Lin, *Angew. Chem., Int. Ed.* **2016**, *55*, 7898.
[50] S. P. Wu, R. Xu, M. J. Lu, R. Y. Ge, J. Iocozzia, C. Han, B. Jiang, Z. Q. Lin, *Adv. Energy Mater.* **2015**, *5*, 1500400.
[51] B. B. Jiang, Y. J. He, B. Li, S. Q. Zhao, S. Wang, Y.-B. He, Z. Q. Lin, *Angew. Chem., Int. Ed.* **2017**, *56*, 1869.
[52] H. Wu, G. Chan, J. W. Choi, I. Ryu, Y. Yao, M. T. McDowell, S. W. Lee, A. Jackson, Y. Yang, L. Hu, Y. Cui, *Nat. Nanotechnol.* **2012**, *7*, 310.
[53] J. Y. Huang, L. Zhong, C. M. Wang, J. P. Sullivan, W. Xu, L. Q. Zhang, S. X. Mao, N. S. Hudak, X. H. Liu, A. Subramanian, H. Fan, L. Qi, A. Kushima, J. Li, *Science* **2010**, *330*, 1515.
[54] S. Chen, Y. L. Xin, Y. Y. Zhou, F. Zhang, Y. R. Ma, H. H. Zhou, L. M. Qi, *J. Mater. Chem. A* **2014**, *2*, 15582.
[55] S. Q. Zhao, Z. W. Wang, Y. J. He, B. B. Jiang, Y. W. Harn, X. Q. Liu, F. Q. Yu, F. Feng, Q. Shen, Z. Q. Lin, *ACS Energy Lett.* **2017**, *2*, 111.

